2D-to-3D reconstruction of carbonate digital rocks using Progressive Growing GAN

Nan You, Yunyue Elita Li, and Arthur Cheng, Department of Civil and Environmental Engineering, National University of Singapore.*

SUMMARY

Digital Rock Physics relies on the availability of high-resolution, large-size 3D digital rock images. In practice, there is always a trade-off between the size and resolution of the acquired images. Moreover, it is time-consuming to acquire high-quality digital rock images using imaging techniques like X-ray micro-Computed Tomography(μCT) and Scanning Electron Microscope (SEM). In this paper, we propose a ML-aided 3D reconstruction method that allows to reduce the sampling rate along the axial direction during image acquisition. Considering the linearity of the latent space learned by a Progressive Growing Generative Adversarial Network (PG-GAN), we reconstruct the missing part between slices scanned at large constant intervals via linear interpolation in the latent space learned by the PG-GAN. We apply our method to reconstructing the 3D image of an Estaillades carbonate rock sample. Both the reconstructed image and the extracted pore network are visually indistinguishable from the ground truth. Overall, our method saves imaging time and cost significantly, enables efficient imaging editing in PG-GAN's linear latent space as well as the utilization of SEM images in 3D reconstruction for enhanced image quality, offers highly efficient compression of the image data, and enlarges the digital rock repository for ML research.

INTRODUCTION

With the advancement of imaging techniques and computation power, Digital Rock Physics (DRP) has become increasingly accurate and effective to characterize the properties of porous media, and thus plays an important role in hydrogeology, petroleum exploitation and production, CO_2 capture and storage (Blunt et al., 2013; Singh et al., 2017; Berg et al., 2017; Nur et al., 2011). Digital rock models are normally built from digital rock images acquired by X-ray micro-Computed Tomography (μCT) or Scanning Electron Microscopes (SEM). μCT imaging provides 3D images with a resolution in micron scale on small core samples whose diameter is in millimeter to centimeter scale. It is limited by the trade-off between the resolution and sample size, meaning that larger sample size is achieved at the cost of lower resolution. SEM compensates the limitations of μCT imaging by offering a higher resolution in sub-micron scale and a larger coverage in centimeter scale. Nevertheless, SEM only images the 2D structure of thin sections, which impedes its potential for DRP studies targeting at 3D flow, mechanical or other properties of rocks.

Since μCT and SEM imaging complement each other, more accurate rock properties can be obtained by combining them to form high-resolution, large-size 3D images. One way to bridge them is to construct 3D images from available 2D images of the cross-sections of rock samples, which is commonly referred to as 2D-to-3D reconstruction (Andrä et al., 2013; Berg et al., 2017; Blunt et al., 2013). There are two types of traditional methods for 2D-to-3D reconstruction: stochastic and process-based methods. The stochastic methods reconstruct 3D digital rocks based on the spatial statistical information contained in the 2D cross-section images (Quiblier, 1984; Adler et al., 1990; Blair et al., 1996). Generally, the stochastic methods take hours to reconstruct a multi-million-voxel digital rock (Pant et al., 2014; Okabe and Blunt, 2004; Čapek et al., 2009). The simplification of rock structure also limits the application of the stochastic methods. Thus, the process-based methods are developed to generate digital rocks with more realistic and complex structure by simulating the sedimentation and diagenesis processes (Øren and Bakke, 2002). However, they do not apply to rocks with unknown sedimentation and diagenesis processes, especially carbonate rocks.

Recently, more and more machine learning (ML) techniques are adopted in 2D-to-3D reconstruction. Although the training of neural networks (NNs) can be very time-consuming and computationally intensive, the NNs, once trained, can be used repeatedly for rapid generation of digital rock images. Most ML-assisted reconstruction methods adopt Generative Adversarial Networks (GAN) (Goodfellow et al., 2014) to generate 2D or 3D digital rock images (e.g., Mosser et al., 2017, 2018; Volkhonskiy et al., 2019; Shams et al., 2020). Bai et al. (2020) proposed a different type of ML-assisted method, which saves imaging cost by reducing the sampling rate along the axial direction in μCT scan. The missing information along the axial direction is restored with a super-resolution convolutional neural networks (SRCNN) (Dong et al., 2015). According to the literature, existing ML-aided approaches for 2D-to-3D reconstruction only succeeded in the reconstruction of small-size digital rocks ($< 200^3$) comprising spherical to ellipsoidal grains. It is doubtful whether existing methods can handle rocks with complex structure, especially carbonate rocks and shales that are abundant in oil and gas reservoirs.

To overcome the challenge of reconstructing large-scale, high-resolution 3D rock images with complex structure seen in carbonates, we propose a ML-aided method to reconstruct 3D rocks from 2D slices scanned at large constant intervals along the axial direction. Our method has three steps. First, a progressive growing GAN (PG-GAN) (Karras et al., 2018) is trained to generate high-quality 2D cross-section images of carbonate rocks from normally distributed latent vectors. Next, the inverse mapping from the scanned 2D slices to the latent vectors is handled by a gradient-descend algorithm. Lastly, the missing slices between the scanned ones are reconstructed by the generator of the PG-GAN from the interpolated latent vectors between the inverted vectors. Our method efficiently reconstructs large-size, high-resolution 3D carbonate images with reduced sampling rate along the axial direction of rock samples during imaging, and thus saves imaging time and cost

10.1190/segam2021-3592148.1

significantly. Additionally, our method enables efficient imaging editing in PG-GAN's latent space, allows the integration of SEM images in 2D-to-3D reconstruction, achieves efficient data compression, and enlarges the digital rock repository for ML research.

METHODOLOGY

In this section, the key techniques employed in our method are explained in detail.

PG-GAN

PG-GAN is an advanced variant of GANs that enables stable synthesis of high-resolution images of great diversity. It is distinguished from other GAN variants by a novel training strategy which is to grow the neural networks progressively during training. As shown in Figure 1, the networks start with low-resolution images of 4×4, and gradually increase to high-resolution images of 1024×1024. At each level of resolution, the neural networks are trained for certain number of iterations before the insertion of convolutional layers operating on larger spatial resolution to the generator and discriminator synchronously. The real images are down-sampled to match current resolution by average pooling. This progressive growing training strategy greatly accelerates the training process since most iterations are performed at resolutions lower than the target resolution ($< 1024^2$) (Karras et al., 2018). It also enables and stabilizes the synthesis of sharp high-resolution images by breaking the challenging end goal into simpler sub-tasks.

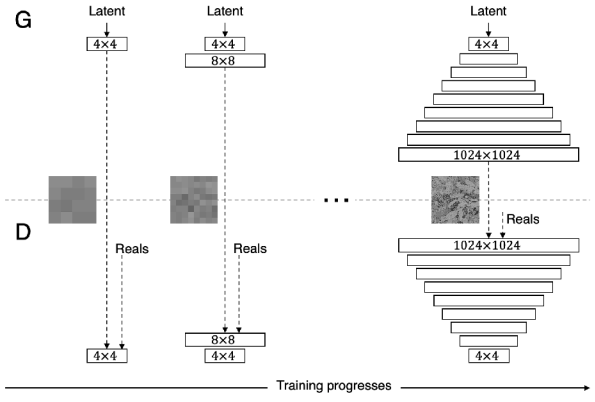

Figure 1: Illustration of the progressive growing training methodology (adapted from Karras et al. (2018)). $\boxed{N \times N}$ refers to convolutional layers operating on $N \times N$ resolution.

GAN inversion

Following the training of PG-GAN is GAN inversion, which is to solve for the latent vectors corresponding to given 2D slices. In order to achieve accurate one-to-one mapping for specific images, we adopt gradient descend algorithms to optimize the latent vectors over the pixelwise image reconstruction error. With $\boldsymbol{X}$, $\boldsymbol{z}$ and G denoting images, latent vectors and the generator, the objective function for GAN inversion is

$$\boldsymbol{z}^* = \underset{\boldsymbol{z}}{argmin} \|\boldsymbol{X} - G(\boldsymbol{z})\|_2^2, (G(\boldsymbol{z}), \boldsymbol{X} \in \mathbb{R}^{N \times N}; \boldsymbol{z} \in \mathbb{R}^d) \quad (1)$$

where $\boldsymbol{z}^*$ represents the inverted latent vector, N and d denote the image resolution and latent vector dimension. Adam optimizer (Kingma and Ba, 2015) is employed to solve Equation 1. Similar to the backpropagation algorithm for network training (Rumelhart et al., 1986), the gradient of the loss function $\|\boldsymbol{X} - G(\boldsymbol{z})\|_2^2$ with respect to $\boldsymbol{z}$ is computed backward through the generator based on the chain rule.

Since the generator is very deep and highly nonlinear, the inversion problem could be highly non-convex. Therefore, we need to initialize $\boldsymbol{z}$ carefully to avoid the inversion to be trapped in local minima. To this end, we initialize $\boldsymbol{z}$ with the one that offers the lowest L_2-norm reconstruction error among 1000 randomly sampled vectors from the latent space.

Latent space interpolation and 3D reconstruction

The fundamental idea of our method is to reconstruct sandwiched layers between scanned layers via interpolation. Experimentally, direct linear interpolation in the image space produces fuzzy and unreliable reconstructions because of the nonlinearity among the digital rock images. An alternative way is to interpolate between the latent vectors learned by PG-GAN, which has been demonstrated to be linear with respect to semantics and attributes in the image space (Radford et al., 2016). Specifically, latent space interpolation can be expressed as

$$\boldsymbol{z}'_j = [1 - \frac{(j-i)}{w}]\boldsymbol{z}_i^* + \frac{(j-i)}{w}\boldsymbol{z}_{i+w}^* \quad (2)$$

with $\boldsymbol{z}'$, w representing the interpolated vector and the scan interval. The subscripts of $\boldsymbol{z}'$ and $\boldsymbol{z}^*$ are the slice indices. The last step is to generate the interpolated images ($\boldsymbol{X}'_j$) from $\boldsymbol{z}'_j$ using the generator of PG-GAN (G).

EXPERIMENT DESIGN

μCT images of an Estaillades carbonate sample (Bultreys, 2016) are used in this paper. They can be freely downloaded from the Digital Rocks Portal (`https://www.digitalrocksportal.org/`). We crop a $1024 \times \times 1024 \times 1720$ cuboid from the center of the 3D μCT image. The voxel length is 3.1 μm along three dimensions.

Assume the extracted 3D cuboid is scanned with a reduced sampling rate of w along z axis, then our method is applied to the reconstruction of the 3D cuboid from a subset of the xy-plane slices denoted with $\boldsymbol{X}_{1+wi}$ ($i \in \mathbb{N}, 1 \leq 1+wi \leq 1720$). Taking the 3D cuboid as the ground truth, we can assess the performance of our method in 3D reconstruction. For simplicity, all 2D slices in the following text are xy-plane slices unless specified otherwise. Our experiment is performed in following steps.

1. Divide the 3D cuboid into a training section (Slice $1 \sim 1530$) and a test section (Slice $1531 \sim 1720$), as shown in Figure 2(b).
2. Train a PG-GAN to synthesize 1024×1024 gray-scale carbonate slices using all slices from the training section and the assumed sparsely scanned slices (separated by an interval of w) from the test section.

10.1190/segam2021-3592148.1

3. Invert for the latent vectors corresponding to the assumed scanned slices $\boldsymbol{X}_{1+wi}$ $(i \in \mathbb{N}, 1 \leq 1+wi \leq 1720)$.
4. Linearly interpolate between the inverted latent vectors and then reconstruct the 3D image by mapping the latent vectors to the image space using the generator of the PG-GAN.
5. Evaluate the reconstruction accuracy by comparing the reconstructed and real images in different plane and sections (i.e., the training and test sections). The test section is designed to examine whether the PG-GAN can recover images outside the training data, and thus assesses the generalizability of our method. Additionally, pore networks are extracted and compared from the real and reconstructed 3D images.

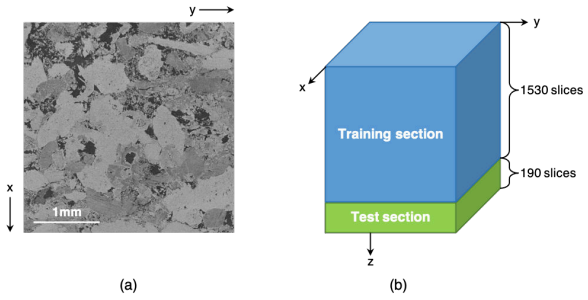

Figure 2: (a) An example of μCT slices in xy plane. (b) A schematic diagram of the training and test data cropped from the raw μCT image of the carbonate sample.

Results

Using μCT images of the Estaillades carbonate sample, a PG-GAN is trained to generate realistic carbonate images from 512-dimensional latent vectors. It takes 10 days to train the PG-GAN on one Tesla V100 GPU. We experimented with various scan intervals (w) ranging from six to 16. The reconstruction accuracy does not present significant improvement as w increases from six to nine. However, as w exceeds nine, unrealistic discontinuities emerge in the reconstructed images. Therefore, we think nine is the optimal interval for this piece of rock sample because it maximizes the efficiency while minimizing the interpolation artifacts.

With w set as the optimal value nine, a total of 192 slices are sampled, denoted by $\boldsymbol{X}_{1+9i}$ $(i = 0, 1, 2, ..., 191)$. Then the latent vectors corresponding to these slices are inverted using the gradient descend method. The average pixelwise L_2-norm reconstruction error between the inverted and real slices is as low as 0.06 after convergence, demonstrating the inversion to be accurate and successful. Figure 3 compares two interpolated slices with the ground truth. Slice 563 and Slice 1715 are the middle slices of certain scan intervals from the training section and the test section, respectively. They are generated by the learned generator given the corresponding interpolated latent vectors. Both interpolated slices (Column 1 of Figure 3) look realistic and visually indistinguishable from the ground truth (Column 2 of Figure 3). As shown in the misfit map on Column 3 of Figure 3, the pixelwise misfits are nearly zero and randomly distributed within pores and grains, with only minor misfits at the pore-grain boundaries. Slice 1715 has a bit higher misfits than Slice 563. This implies that the reconstruction error can be further reduced with more abundant training data.

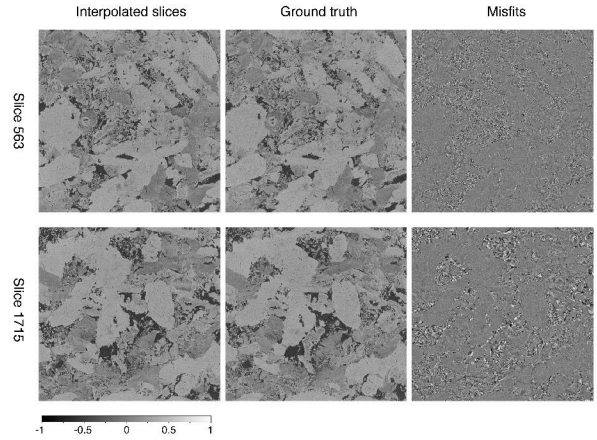

Figure 3: Comparison of the interpolated slices ($\boldsymbol{X}_{rec}$) on the first column and the ground truth ($\boldsymbol{X}_{true}$) on the second column for Slices 563 and 1715 from the training and test sections, respectively. The misfits ($\boldsymbol{X}_{rec} - \boldsymbol{X}_{true}$) are shown on the third column. All slices are normalized between -1 and 1 with equation $\boldsymbol{X}_{norm} = \boldsymbol{X}/127.5 - 1$. The gray-scale colorbar for the slices and misfits are shown on the bottom of the figure.

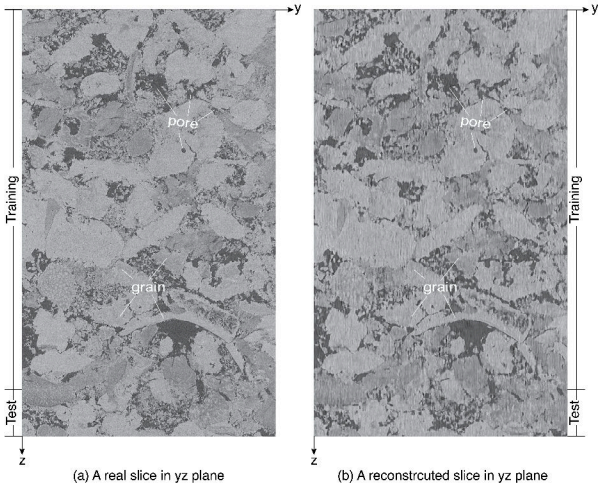

Figure 4: Comparison of a real slice (a) and the corresponding reconstructed slice (b) in the yz plane.

The 3D digital rock image is achieved by the concatenation of reconstructed 2D slices along z axis. Figure 4 compares one reconstructed slice in the yz plane with the ground truth. As pointed out in Figure 4, pores and grains are well restored in the reconstructed slice. The interpolation process in the latent space slightly degrades the image resolution and causes mild linear artifacts in the reconstructed slice. There is nearly no difference in the reconstruction performance between the training and test sections, demonstrating satisfying generalizability of our method.

10.1190/segam2021-3592148.1

Flow simulations through the complex pore networks of digital rocks is an important application of DRP to estimate fluid transport properties of rocks, including relative permeability and capillary pressure (Berg et al., 2017). Therefore, accurate reconstruction of pore networks warrants accurate estimation of fluid transport properties of rocks. Here the pore networks extracted from the real and reconstructed digital rock images are compared. Since the entire pore network is too large to be visualized clearly, we only present a $512 \times 512 \times 512$ subnetwork from the center of the rock in Figure 5. Generally, the real and reconstructed pore networks look similar and consistent, especially for large pores in red. Apart from that, their effective porosities are nearly the same, which are 11.1% and 11.2% for the real and reconstructed pore networks, respectively.

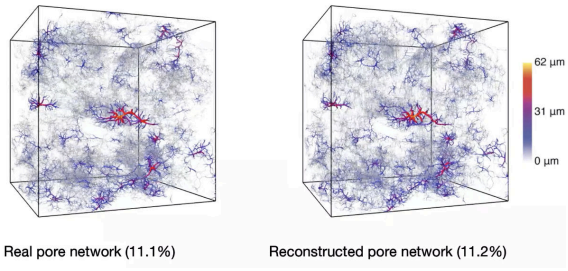

Figure 5: Comparison of the connected pore networks extracted from the center of the real (a) and reconstructed rock (b). Thickness and color of the tubes represent the average radius of the pores on both ends of the tubes.

Discussion

Our method deals with 2D xy-plane slices all the time. The structural information in z axis is achieved by linear interpolation between the latent vectors corresponding to the sparsely spaced xy-plane slices. This proves that semantic concepts and pixel patterns are encoded linearly in the latent space learned by the PG-GAN, which has been proven and utilized in previous studies (e.g., Radford et al., 2016). Thus, image editing might become simpler and more efficient in the latent space (Zhu et al., 2016; Perarnau et al., 2016; Zhu et al., 2020). We might be able to simulate natural processes like rock deformation, cementation and failure by linear transformation of the latent vectors.

Our method applies under conditions that sparsely spaced 2D cross-section images of the same rock are available. A recent SEM imaging technique satisfies such condition, which is focused ion beam SEM (FIB-SEM). It gradually etches thin slices from the sample, while the newly exposed surface is sequentially acquired by SEM (Briggman and Bock, 2012). The imaging depth of FIB-SEM is limited by the acquisition time and memory (Kelly et al., 2016). Therefore, our method has great potential to reconstruct higher-resolution, larger-size 3D digital rock images from FIB-SEM images that sampled sparsely along depth than 3D reconstructions from μCT images.

Data compression is an additional benefits brought by our method. In our experiment, a $1720 \times 1024 \times 1024$ image are represented with 192 512-dimensional latent vectors. If the image data and the latent vectors are respectively stored as uint8 and float32 data, the data size would be compressed from 1720 MB to 0.375 MB using our method. Although the trained PG-GAN consumes 261 MB memory, it is much smaller than the saved memory and would become increasingly insignificant as the same PG-GAN is applied to the compression of other carbonate images repeatedly.

The lack of training data is a common reason that hinders ML applications to DRP, as mentioned in many studies (e.g., Cang et al., 2018; Karimpouli and Tahmasebi, 2019; Santos et al., 2020). We demonstrate that the PG-GAN can be trained to generate realistic high-resolution carbonate images. Similarly, more PG-GANs can be trained to generate cross-section images of other rock types. Such a repository of PG-GANs can be used for rapid generation of any required number of rock images at negligible computation cost, and thus greatly enlarges the digital rock repository for future ML research.

In the training of PG-GAN, no structural information in z axis is considered. One way to include information from the third dimension is to directly train a 3D GAN to synthesize 3D images. However, such approach is impractical since 3D GANs have a lot more trainable parameters and consume much more memory and computation power compared to 2D GANs, making the training process extremely slow and even prone to Out Of Memory (OOM) issue. Therefore, how to consider structural information in all dimensions while maintaining reasonable computational and memory cost requires breakthroughs in the neural network architecture or the training strategy design.

Conclusions

In this paper, we proposed a novel approach to reconstruct high-resolution large-size 3D digital rock images from 2D slices scanned at large constant intervals along the axial direction of the rock sample to save imaging cost and time. We accurately reconstruct the 3D microstructure of a carbonate rock sample and greatly compress the image data from 1720 MB to 0.375 MB. Our approach also demonstrates the feasibility of efficient editing of digital rock images in the latent space and enables the utilization of SEM images in 3D reconstruction. The PG-GANs have the potential to enlarge the digital rock database and contribute to the advancement of big data in DRP.

ACKNOWLEDGMENTS

The authors would like to thank for the financial supports from the Singapore Economic Development Board (EDB) Petroleum Engineering Professorship. The digital rock images can be retrieved from `https://www.digitalrocksportal.org/projects/58`. The 3D reconstruction code is available from `https://doi.org/10.5281/zenodo.4437911` (You, 2021).

10.1190/segam2021-3592148.1

REFERENCES

Adler, P., C. G. Jacquin, and J. Quiblier, 1990, Flow in simulated porous media: International Journal of Multiphase Flow, **16**, 691–712, doi: https://doi.org/10.1016/0301-9322(90)90025-E.

Andrä, H., N. Combaret, J. Dvorkin, E. Glatt, J. Han, M. Kabel, Y. Keehm, F. Krzikalla, M. Lee, C. Madonna, and M. Marsh, 2013, Digital rock physics benchmarks—Part I: Imaging and segmentation: Computers & Geosciences, **50**, 25–32, doi: https://doi.org/10.1016/j.cageo.2012.09.005.

Bai, Y., V. Berezovsky, and V. Popov, 2020, Digital core 3d reconstruction based on micro-ct images via a deep learning method: 2020 International Conference on High Performance Big Data and Intelligent Systems (HPBD&IS), IEEE, 1–6.This query was generated by an automatic reference checking system. This reference could not be located in the databases used by the system. While the reference may be correct, we ask that you check it so we can provide as many links to the referenced articles as possible.

Berg, C. F., O. Lopez, and H. Berland, 2017, Industrial applications of digital rock technology: Journal of Petroleum Science and Engineering, **157**, 131–147, doi: https://doi.org/10.1016/j.petrol.2017.06.074.

Blair, S. C., P. A. Berge, and J. G. Berryman, 1996, Using two-point correlation functions to characterize microgeometry and estimate permeabilities of sandstones and porous glass: Journal of Geophysical Research, Solid Earth, **101**, 20359–20375, doi: https://doi.org/10.1029/96JB00879.

Blunt, M. J., B. Bijeljic, H. Dong, O. Gharbi, S. Iglauer, P. Mostaghimi, A. Paluszny, and C. Pentland, 2013, Pore-scale imaging and modelling: Advances in Water resources, **51**, 197–216, doi: https://doi.org/10.1016/j.advwatres.2012.03.003.

Briggman, K. L., and D. D. Bock, 2012, Volume electron microscopy for neuronal circuit reconstruction: Current Opinion in Neurobiology, **22**, 154–161, doi: https://doi.org/10.1016/j.conb.2011.10.022.

Bultreys, T., 2016, Estaillades carbonate #2, http://www.digitalrocksportal.org/projects/58.

Cang, R., H. Li, H. Yao, Y. Jiao, and Y. Ren, 2018, Improving direct physical properties prediction of heterogeneous materials from imaging data via convolutional neural network and a morphology-aware generative model: Computational Materials Science, **150**, 212–221, doi: https://doi.org/10.1016/j.commatsci.2018.03.074.

Čapek, P., V. Hejtmánek, L. Brabec, A. Zikánová, and M. Kočiřík, 2009, Stochastic reconstruction of particulate media using simulated annealing: Improving pore connectivity: Transport in Porous Media, **76**, 179–198, doi: https://doi.org/10.1007/s11242-008-9242-8.

Dong, C., C. C. Loy, K. He, and X. Tang, 2015, Image super-resolution using deep convolutional networks: IEEE transactions on Pattern Analysis and Machine Intelligence, **38**, 295–307, doi: https://doi.org/10.1109/TPAMI.2015.2439281.

Goodfellow, I., J. Pouget-Abadie, M. Mirza, B. Xu, D. Warde-Farley, S. Ozair, A. Courville, and Y. Bengio, 2014, Generative adversarial nets: Advances in Neural Information Processing Systems, 2672–2680.

Karimpouli, S., and P. Tahmasebi, 2019, Image-based velocity estimation of rock using convolutional neural networks: Neural Networks, **111**, 89–97, doi: https://doi.org/10.1016/j.neunet.2018.12.006.

Karras, T., T. Aila, S. Laine, and J. Lehtinen, 2018, Progressive growing of gans for improved quality, stability, and variation: Presented at the International Conference on Learning Representations.

Kelly, S., H. El-Sobky, C. Torres-Verdín, and M. T. Balhoff, 2016, Assessing the utility of fib-sem images for shale digital rockphysics: Advances in Water Resources, **95**, 302–316, doi: https://doi.org/10.1016/j.advwatres.2015.06.010.

Kingma, D. P., and J. L. Ba, 2015, Adam: A method for stochastic optimization: Presented at the International Conference on Learning Representations 2015.

Mosser, L., O. Dubrule, and M. J. Blunt, 2017, Reconstruction of three-dimensional porous media using generative adversarial neural networks: Physical Review E, **96**, 043309, doi: https://doi.org/10.1103/PhysRevE.96.043309.

Mosser, L., O. Dubrule, and M. J. Blunt, 2018, Stochastic reconstruction of an oolitic limestone by generative adversarial networks: Transport in Porous Media, **125**, 81–103, doi: https://doi.org/10.1007/s11242-018-1039-9.

Nur, A., T. Vanorio, and E. Diaz, 2011, Effects of carbon dioxide injection in reactive carbonates: Computational rock physics basis for time-lapse monitoring: Presented at the SPE/DGS Saudi Arabia Section Technical Symposium and Exhibition, SPE.

Okabe, H., and M. J. Blunt, 2004, Prediction of permeability for porous media reconstructed using multiple-point statistics: Physical Review E, **70**, 066135, doi: https://doi.org/10.1103/PhysRevE.70.066135.

Pant, L. M., S. K. Mitra, and M. Secanell, 2014, Stochastic reconstruction using multiple correlation functions with different-phase-neighbor-based pixel selection: Physical Review E, **90**, 023306, doi: https://doi.org/10.1103/PhysRevE.90.023306.

Perarnau, G., J. Van De Weijer, B. Raducanu, and J. M. Álvarez, 2016, Invertible conditional gans for image editing: arXiv preprint arXiv:1611.06355.

Radford, A., L. Metz, and S. Chintala, 2016, Unsupervised representation learning with deep convolutional generative adversarial networks: Presented at the International Conference on Learning Representations 2016.

Øren, P.-E., and S. Bakke, 2002, Process based reconstruction of sandstones and prediction of transport properties: Transport Inporous Media, **46**, 311–343, doi: https://doi.org/10.1023/A:1015031122338.

Rumelhart, D. E., G. E. Hinton, and R. J. Williams, 1986, Learning representations by back-propagating errors: Nature, **323**, 533–536, doi: https://doi.org/10.1038/323533a0.

Santos, J. E., D. Xu, H. Jo, C. J. Landry, M. Prodanović, and M. J. Pyrcz, 2020, Poreflow-net: A 3d convolutional neural network to predict fluid flow through porous media: Advances in Water Resources, **138**, 103539, doi: https://doi.org/10.1016/j.advwatres.2020.103539.

Shams, R., M. Masihi, R. B. Boozarjomehry, and M. J. Blunt, 2020, Coupled generative adversarial and auto-encoder neural networks to reconstruct three-dimensional multi-scale porous media: Journal of Petroleum Science and Engineering, **186**, 106794, doi: https://doi.org/10.1016/j.petrol.2019.106794.

Singh, K., H. Menke, M. Andrew, Q. Lin, C. Rau, M. J. Blunt, and B. Bijeljic, 2017, Dynamics of snap-off and pore- filling events during two-phase fluid flow in permeable media: Scientific Reports, **7**, 1–13, doi: https://doi.org/10.1038/s41598-017-05204-4.

Volkhonskiy, D., E. Muravleva, O. Sudakov, D. Orlov, B. Belozerov, E. Burnaev, and D. Koroteev, 2019, Reconstruction of 3d porous media from 2d slices: arXiv preprint arXiv:1901.10233.

You, N., 2021, Nannanyou/3D-digital-rock-reconstruction-using-PGGAN.

Zhu, J., Y. Shen, D. Zhao, and B. Zhou, 2020, In-domain gan inversion for real image editing: Computer Vision – ECCV 2020, Springer International Publishing, 592–608.

Zhu, J.-Y., P. Krähenbühl, E. Shechtman, and A. A. Efros, 2016, Generative visual manipulation on the natural image manifold: European Conference on Computer Vision, Springer, 597–613.

10.1190/segam2021-3592148.1